SANDIA REPORT
SAND2019-13705
Printed Click to enter a date

Sandia National Laboratories

Near-Infrared Nanophotonics through Dynamic Control of Carrier Density in Conducting Ceramics

Michael G. Wood, Salvatore Campione, Ting S. Luk, Joel R. Wendt, Joshua Shank, Victoria Sanchez, and Darwin K. Serkland

Prepared by
Sandia National Laboratories
Albuquerque, New Mexico
87185 and Livermore,
California 94550

Issued by Sandia National Laboratories, operated for the United States Department of Energy by National Technology & Engineering Solutions of Sandia, LLC.

Available to DOE and DOE contractors from
U.S. Department of Energy
Office of Scientific and Technical Information
P.O. Box 62
Oak Ridge, TN 37831

Telephone: (865) 576-8401
Facsimile: (865) 576-5728
E-Mail: reports@osti.gov
Online ordering: http://www.osti.gov/scitech

Available to the public from
U.S. Department of Commerce
National Technical Information Service
5301 Shawnee Rd
Alexandria, VA 22312

Telephone: (800) 553-6847
Facsimile: (703) 605-6900
E-Mail: orders@ntis.gov
Online order: https://classic.ntis.gov/help/order-methods/

ABSTRACT

Major breakthroughs in silicon photonics often come from the integration of new materials into the platform, from bonding III-Vs for on-chip lasers to growth of Ge for high-speed photodiodes. This report describes the integration of transparent conducting oxides (TCOs) onto silicon waveguides to enable ultra-compact (<10 μm) electro-optical modulators. These modulators exploit the "epsilon-near-zero" effect in TCOs to create a strong light-matter interaction and allow for a significant reduction in footprint. Waveguide-integrated devices fabricated in the Sandia Microfab demonstrated gigahertz-speed operation of epsilon-near-zero based modulators for the first time. Numerical modeling of these devices matched well with theory and showed a path for significant improvements in device performance with high-carrier-mobility TCOs such as cadmium oxide. A cadmium oxide sputtering capability has been brought online at Sandia; integration of these high mobility films is the subject of future work to develop and mature this exciting class of Si photonics devices.

ACKNOWLEDGEMENTS

We thank the NMRF LDRD committee both for funding this program and for their guidance and suggestions along the way. We also thank Gordon Keeler, the initial PI for this program for laying the groundwork for its success.

We further acknowledge the hard work of fabrication technologists including S. Parameswaran ("Para"), Travis Young, Kate Musick, Joe Bischoff, Lily Ruiz, and Tony James. The device results reported here would not be possible without their assistance.

CONTENTS

LIST OF FIGURES

LIST OF TABLES

This page left blank

ACRONYMS AND DEFINITIONS

Abbreviation	Definition
APD	Avalanche photodiode
Au	Gold
AZO	Aluminum-doped zinc oxide
CdO	Cadmium oxide
CINT	Center for Integrated Nanotechnology
dB	Decibels
ENZ	Epsilon-near-zero
FDTD	Finite-difference time-domain
In_2O_3	Indium oxide
MgO	Magnesium oxide
MSE	Mean-squared error
PIC	Photonic integrated circuit
RF	Radiofrequency
Si	Silicon
TCO	Transparent conducting oxide
TiN	Titanium nitride
Y	Yttrium

1. INTRODUCTION

Electro-optical modulators are critical elements of optical communication systems which encode electrical data onto an optical signal for transmission or processing. In the rapidly developing field of silicon (Si) photonics, modulation is typically achieved through the relatively weak plasma dispersion effect by injecting or deleting carriers [1] by creating a *p-i-n* junction through ion implantation of the Si waveguide or surrounding regions. Mach-Zehnder interferometer modulators based on this effect have typical lengths on the order of 500 μm due to an induced change in refractive index on the order of 0.01 [2]. This footprint can be significantly reduced by integrating the junction into a resonant structure [3,4] at the expense of a correspondingly smaller optical bandwidth. The tradeoff between physical size and optical bandwidth can be avoided by instead integrating new materials with significantly stronger light-matter interaction and corresponding refractive index modulation. This report presents results of a project investigating epsilon-near-zero (ENZ) modulation in transparent conducting oxides (TCOs) integrated in close proximity to Si photonic waveguides. Through proper design, these ENZ modulators show refractive index changes on the order of 1, allowing for significant optical modulation with active devices with lengths <10 μm. Reduction of device size is important for realizing the integration densities promised by Si photonics and a broad optical bandwidth implies tolerance to fabrication and environmental/thermal variations. The principal of operation of these ENZ devices is described below and further details are available in [5] and references therein.

A schematic of a TCO-based ENZ modulator integrated on a Si waveguide is given in Figure 1-1(a). The active region is a capacitive structure with an oxide bilayer sandwiched between the lower doped-Si contact and the top gold (Au) gate electrode. The oxide bilayer includes both a TCO and a hafnia dielectric. In the unbiased state (Figure 1-1(b)), the TCO acts as a low-loss dielectric, the optical field is shared between the two oxide layers, and the insertion loss is relatively low. Under bias (Figure 1-1(c)), electrons accumulate at the interface of the TCO and hafnia, forming an approximately 1 nm thick accumulation layer with a charge density on the order of 1e20 cm^{-3} [5]. This large charge density induces a change in the dielectric function (Figure 1-1(d)) of the TCO layer such that the permittivity (epsilon) of the accumulation layer approaches zero at the operating wavelength of the Si waveguide. This ENZ effect results in significant confinement of the optical field inside the accumulation layer while simultaneously increased absorption in this layer and, thus, creates a high loss state. By electrically controlling the bias voltage, the device can be switched between these two states to achieve electro-optical modulation.

The goals of this LDRD program were to better understand the operation of ENZ modulators through experimentation, material characterization, and modeling and use that learning to design and demonstrate a new class of devices with improved performance and increased functionality. Overall, we have achieved these goals and have been subsequently funded to continue development of these devices. The remainder of this report is organized as follows: Section 2 describes and provides references to our published work during this program, Section 3 gives details on our work to reduce Si waveguides losses and design new device configurations, Section 4 covers the deposition and characterization of TCO materials including indium oxide (In_2O_3) and cadmium oxide (CdO), and Section 5 concludes the report and describes areas for future work.

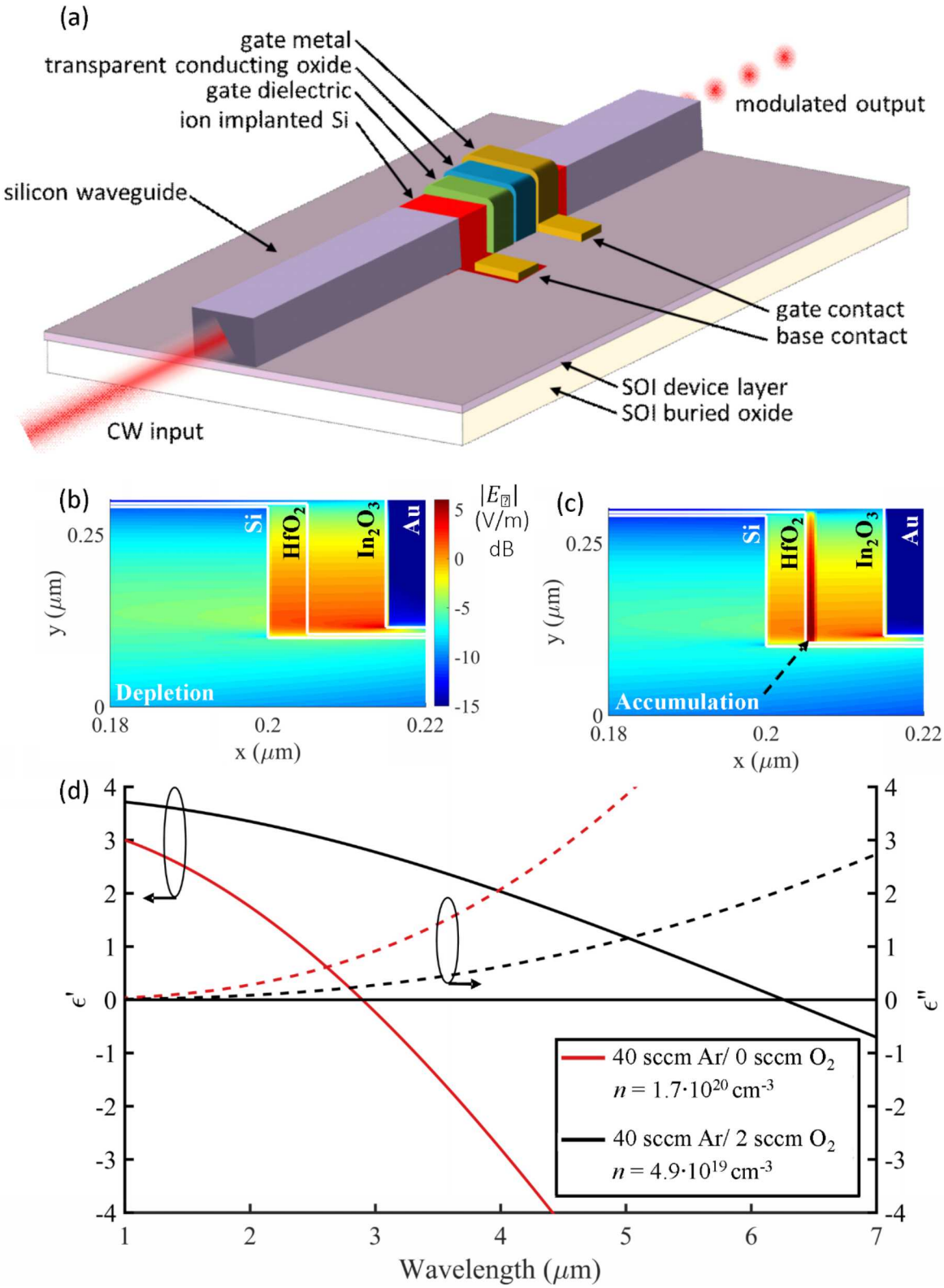

Figure 1-1. Overview of ENZ modulator operation. (a) Schematic of the device geometry. (b) Field confinement in the unbiased state is balanced between the TCO and hafnia oxide bilayer. (c) Field confinement in the biased state is strongly enhanced in the thin accumulation layer of the TCO. (d) Drude model describes the TCO permittivity as a function of carrier density.

2. OVERVIEW OF PUBLISHED WORK

Many of the results of this program have been published and/or presented at conferences. Rather than repeat those results in this report, this section briefly describes these publications and provides references to the reader.

2.1. Experimental demonstration of high-speed ENZ modulation

Under this program we reported the first experimental demonstration of GHz-speed modulation in ENZ devices incorporated on Si photonics waveguides. Initial data was presented over three conference talks [6], [7], [8], with a full report in a paper published in *Optica* [5]. We reported optically broadband (>60 nm) modulation in a 5 μm long, non-resonant device and data transmission at 2.5 Gbps.

2.2. Modeling of amplitude and phase ENZ modulators

Numerical modeling of ENZ modulators was a significant thrust of this program as there were few reports on this topic in the literature. The primary modeling technique used in the program was finite-difference time-domain (FDTD) using software by Lumerical. Modeling results of amplitude modulation in ENZ devices are presented in [9], [10], [11], and [12].

Additional modeling efforts focused on demonstrating phase modulators based on the ENZ platform. These results were presented in [13] and [14]. Notably, it was demonstrated that efficient phase modulation is only possible in TCO materials with sufficiently high carrier mobility such as cadmium oxide (CdO).

2.3. Academic Alliance publications

This program included an Academic Alliance collaboration with Prof. Alexandra Boltasseva of Purdue University. Her group focused on developing more exotic TCC materials such as titanium nitride (TiN) and aluminum-doped zinc oxide (AZO). Results supported by this collaboration have been reported in two conference publications: [15] and [16].

Additional work with Purdue focused on characterization of yttrium(Y)-doped CdO films deposited at Sandia. The results of this work have recently been accepted for publication [17].

This page left blank

3. DEVELOPMENT OF SI WAVEGUIDE PROCESS IN SNL MICROFAB

Initial work developing ENZ waveguide modulators began under a previous Exploratory Express LDRD that laid the groundwork for this program. While these initial devices did show modulation, insertion losses were typically very high (>30 decibels (dB)) even for test waveguide devices without integrated TCO films and electrodes. Coupling to these devices was achieved with grating couplers [18] which ultimately limited the demonstrated optical bandwidth in [5] rather than a bandwidth limitation of the ENZ physics. Several improvements to the fabrication process were implemented to address these limitations and produce devices that operate over a wider optical bandwidth and with less insertion loss.

Notably, all devices fabricated under this program were processed in the Sandia Microfab and Center for Integrated Nanotechnology (CINT) Integration Lab rather than the Sandia SiFab. While there are existing low-loss processes for fabricating waveguides in the SiFab, we utilized these alternative cleanrooms since they allowed integration of a wider pallet of materials such as In_2O_3 and Au and they can allow for rapid turn-around times to iterate processes steps.

3.1. Reduction of propagation loss in Si waveguides

Reduction of waveguide propagation losses occurred on two fronts: (1) reducing sidewall roughness after dry etching and (2) removing Ge contamination. Sidewall roughness was reduced by introducing a resist reflow step and optimizing the inductively-coupled plasma reactive-ion etch (ICP-RIE) chemistry and pressure following the process developed in [19]. The improvement in sidewall roughness can be seen from panel (a) to (c) in Figure 3-1.

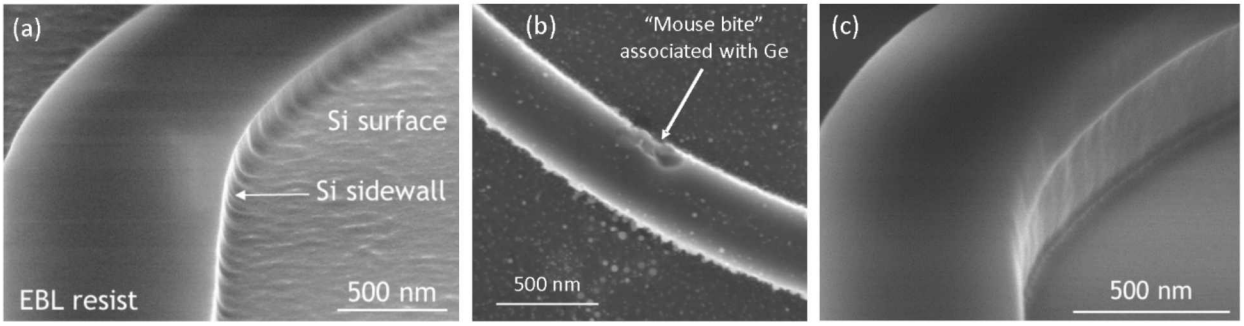

Figure 3-1. Progress on Si waveguide fabrication process over the course of the program. (a) Typical waveguide at start of program start. (b) Waveguide damage after annealing Ge contaminated samples. (c) Typical waveguides at end of program after annealing.

Based on the results of [19], we would expect the initial sidewall roughness to account for approximately 10 dB/cm of propagation loss. However, analysis of the baseline waveguides showed a propagation loss of >300 dB/cm; losses at this level are typically due to absorption in the waveguide material rather than scattering. Using energy-dispersive x-ray spectroscopy (EDX), Ge contamination was found throughout the prior lot of samples. Evidence for this contamination and the associated waveguide damage is shown in Figure 3-2 and Figure 3-1(b).

By stepping through the fabrication process and taking scanning electron microscope (SEM) images and EDX measurements after each process, it was determined that the Ge contamination occurred during a high temperature annealing step after ion implantation. In particular, the source was tracked to a specific shared handle wafer which was potentially contaminated with Ge through improper heating of a prior sample. Ge is a particularly deleterious contaminate for Si waveguides as Ge is typically used in Si photonics as a detector material due to its high absorption in the 1550 nm telecommunications band [20]. Issues with Ge contamination and the resultant waveguide damage were entirely corrected by using a dedicated handle wafer for the high temperature anneals needed after ion implantation.

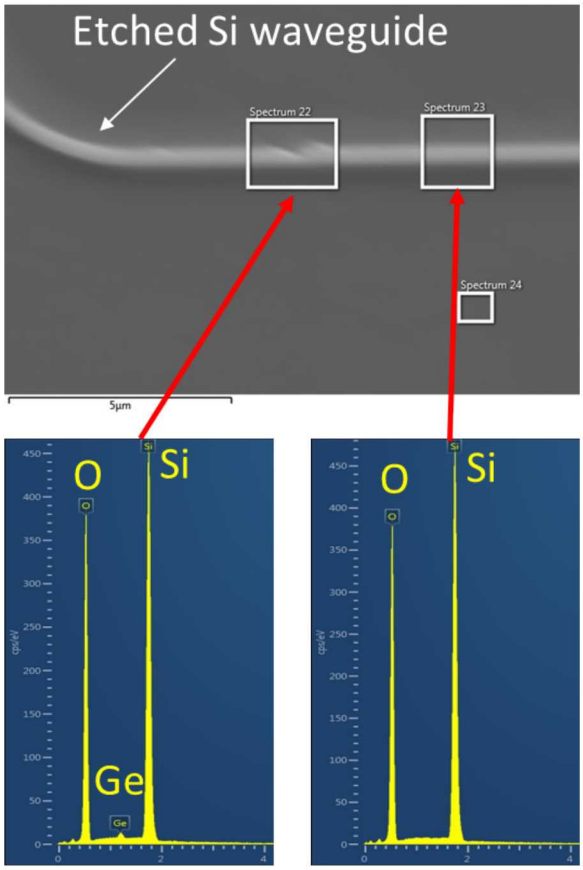

Figure 3-2. EDX analysis of annealed waveguides showing evidence of Ge contamination.

Finally, the fiber-to-chip grating couplers were replaced with inverse waveguide tapered couplers to reduce coupling loss and increase optical bandwidth. An image of a fabricated coupler is shown in Figure 3-3(b) and details on a similar coupler design are reported in [21]. A test vehicle was fabricated to demonstrate these improvements and ensure that the Ge contamination issue had been corrected. An image of the fabricated chip is shown in Figure 3-3(a).

The devices were characterized using the measurement system described in the next section. The results of a cutback method measurement [19], shown in Figure 3-3(c) show a dramatic reduction in both propagation and coupling loss. We measured a propagation loss of 1.8 dB/cm and coupling loss of 3.7 dB/connection. Notably, these values give a total insertion loss of less than 20 dB, as

indicated by the black line in Figure 3-3(c) meaning that measurement will not require the use of an avalanche photodiode (APD).

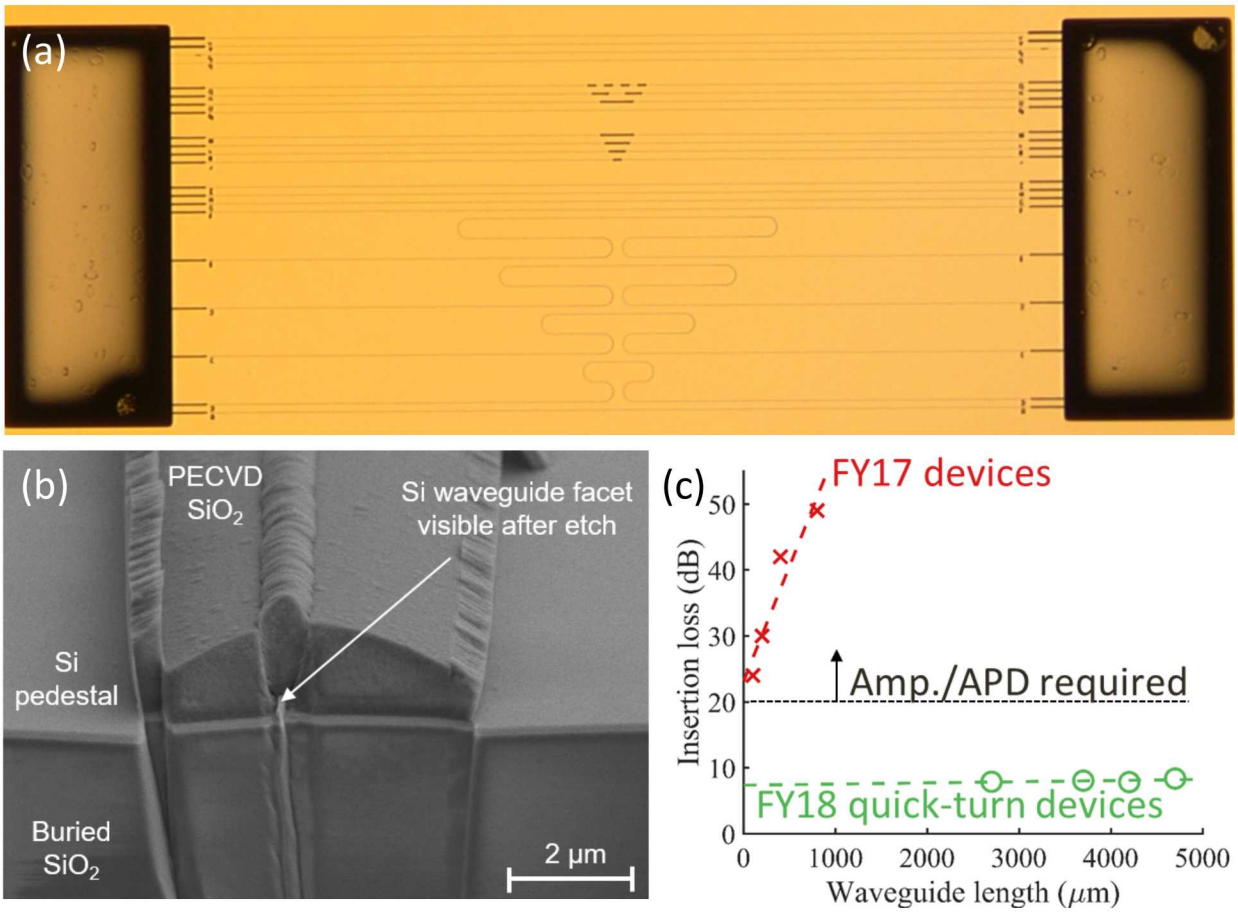

Figure 3-3. Propagation loss reduction test vehicle results. (a) Top-down view of fabricated waveguide array. (b) Etched optical input facet. (c) Cutback measurement results.

3.2. Installation of free-space coupling measurement system

A new fiber-to-chip coupling system was designed and installed to allow for efficient, optically broadband coupling and radiofrequency (RF) electrical driving of the ENZ modulator devices. The system is capable of coupling light into the chip from three different infrared lasers collectively covering the 1250-1750 nm wavelength band. Additional optical ports allow fiber coupling at 980 nm and 635 nm. A variety of detectors can be used to measure throughput and high-speed modulation. A schematic diagram of the final setup is shown in Figure 3-4. Figures 3-5(a) and (b) provide a photograph of the system and an image of the chip while landing an RF probe on a modulator device, respectively.

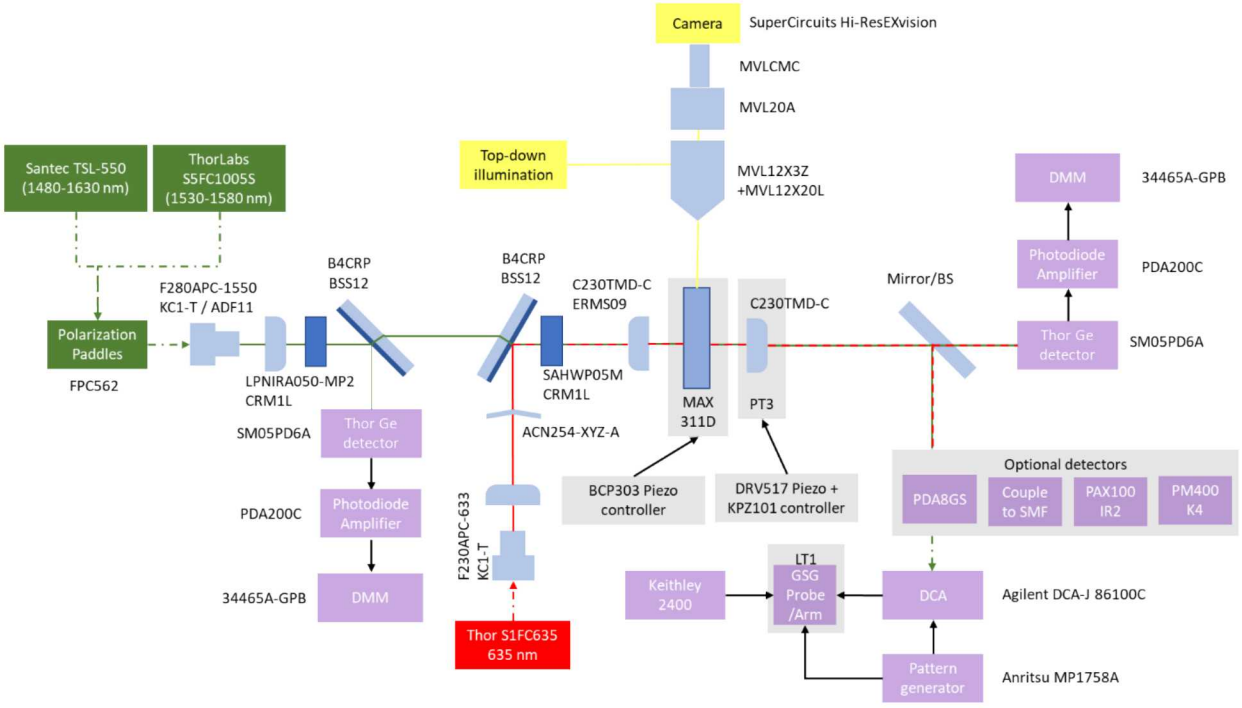

Figure 3-4. Schematic diagram of the fiber-to-free-space coupling system.

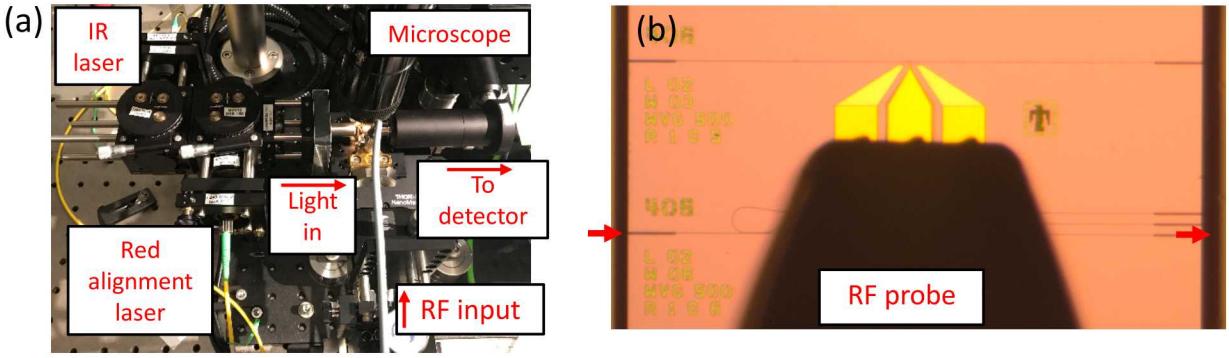

Figure 3-5. (a) Photograph of the measurement system. (b) View from top-down camera of RF probes landing on a modulator sample.

3.3. Development of new modulator mask and improved fabrication process

With the improvements to the waveguide process demonstrated, we set out to integrate these changes into the process flow while also reducing the size of the electrical gates to reduce parasitic capacitance. In addition, the RF driving resistance was decreased across a series of samples through higher ion implantation doses. The parasitic capacitance was decreased by using electron-beam lithography rather than photolithography to both reduce the required gate width through alignment to the patterned waveguides to better than 100 nm. In total, we expect a >10x reduction in the driving circuit RC time constant and a corresponding increase in data rate compared to [5].

These changes were implemented through the generation of a new mask set, shown in Figure 3-6(a). In addition to a variety of different ENZ modulator designs, more complex structures such as pulse amplitude modulation (PAM) devices (shown in Figure 3-6(b)) and ENZ modulators integrated into Mach-Zehnder interferometers were also included to demonstrate advanced modulation schemes. Figure 3-6(c) shows an angled-view SEM image of a device at the end of the fabrication process. Here we see the summation of all of the changes to the fabrication process including improved sidewall roughness on the waveguides and reduced gate size.

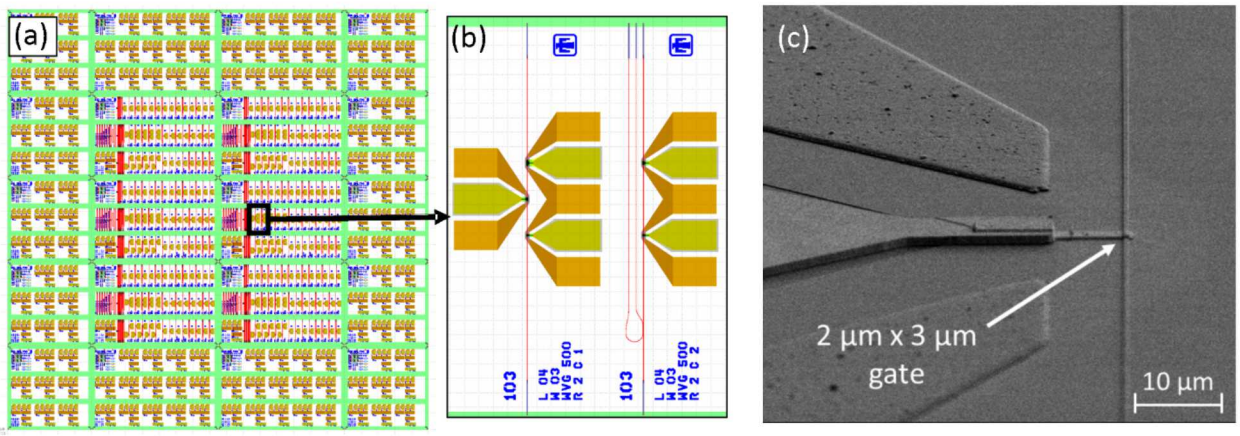

Figure 3-6. Results of updated mask and fabrication process. (a) Image of new photomask. Outer die are RF test structures and inner die have a variety of waveguide and modulator designs. (b) Close-up view of a PAM device implemented on the mask set. (c) Angled-view SEM image of a fabricated device showing good alignment of the large contacts patterned by photolithography and the waveguide and metal gates patterned with two different e-beam lithography processes.

While fabrication of multiple samples with this new process was nearly completed by the conclusion of the program, an issue with the final etch tool used to define the optical facets prevented their measurement. One device was etched and tested but showed very poor optical coupling due to significant scattering from the roughly etched facet. Future work includes polishing the waveguide facets on this chip and etching the remaining samples after the etch recipe is brought back online. Testing these devices should be straightforward once they are ready thanks to the newly installed measurement system and will be performed under follow-on funding.

This page left blank

4. DEPOSITION AND CHARACTERIZATION OF TCO FILMS

As this program focused on exploring ENZ effects in TCO thin films integrated on a Si photonic integrated circuit (PIC), significant effort was devoted to depositing and characterizing high quality TCO films. These efforts were focused initially on In_2O_3 and later on CdO for its higher carrier mobility and potential for improved performance for both amplitude and phase modulators.

4.1. Sputtering of In_2O_3 and CdO

The deposition and annealing of high quality In_2O_3 thin films were key developments of the high speed ENZ modulator reported in [5]. That publication includes details on the film properties and ability to tune the static ENZ wavelength with the O_2 flow during sputtering. These films were deposited in the Sandia Microfab.

Cadmium oxide deposition was performed in a custom-built sputtering chamber designed to match the high carrier mobilities reported by the Jon-Paul Maria group [22]. The sputtering system, shown in Figure 4-1, is capable of depositing CdO doped with Y and magnesium oxide (MgO). The ability to deposit a CdO/MgO bilayer is interesting from a fabrication standpoint since MgO can act as the gate oxide in the capacitor stack. Characterization results of CdO and MgO films deposited with this system are presented in section 4.3 and additional details about the CdO films are provided in [17].

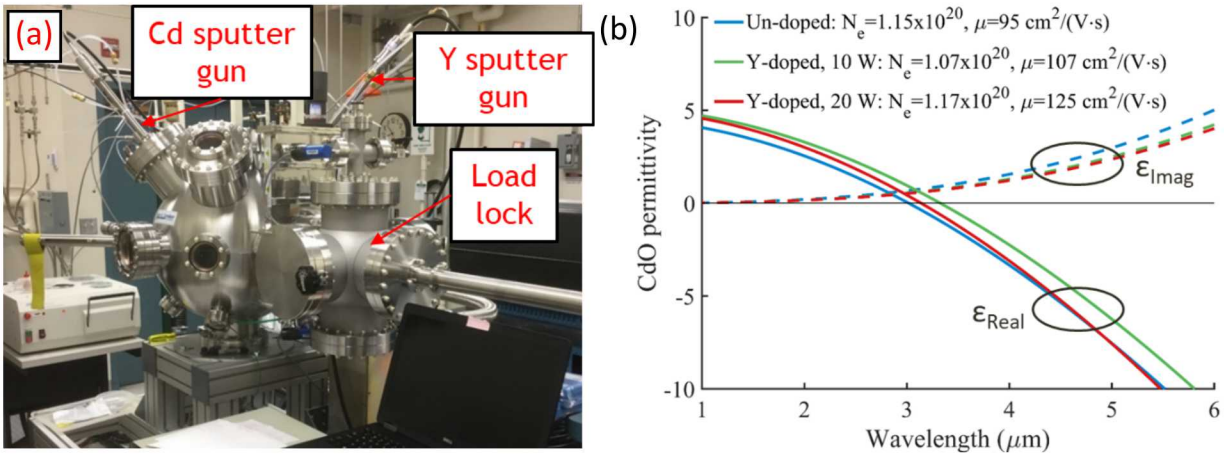

Figure 4-1. (a) Cadmium oxide sputtering system. (b) Ellipsometry results showing the ability to tune the ENZ wavelength and carrier mobility with Y doping.

4.2. Ellipsometric characterization of polycrystalline In_2O_3

Spectroscopic ellipsometry is widely used to study optical properties of materials. It measures the reflectivity ratio of *p*- and *s*-polarization with a known incident mixture of *p*- and *s*- polarized light. Using the Fresnel equation, this ratio can be written as $r_p/r_s = \exp(i\Delta)\cdot\tan\psi$, where the angles Δ and ψ are the raw data of an ellipsometric measurement. Ellipsometry characterization is important to optimize and calibrate the deposition process of the conductive oxide to create the necessary carrier density and mobility for producing the accumulation/depletion layer needed for the optical modulator during voltage bias. During the development phase, such characterization was used to

determine the optimal processing parameters. For subsequent sample fabrications, it is used to ensure the processing tools are producing the material properties needed.

For all the 2017 and 2019 samples tested, we found the carrier concentration is quite sensitive to the deposition condition and the amount of O_2 in the base pressure during sputtering deposition. In general, higher O_2 concentration produces lower carrier density films. Of the 0, 1.25, 2.5 and 4% O_2 concentrations in Ar pressure, the highest carrier concentrations obtained are $5x10^{20}$ cm^{-3} and $4x10^{19}$ cm^{-3} for 0 and 4% O_2 respectively. The mobilities of these samples are typically about 3-10 cm^2/Vs. Literature has shown mobilities of In_2O_3 film can reach as high as 100 cm^2/Vs [23]. From these samples, the mobilities are fairly independent to the annealing environment: air ambient versus N_2.

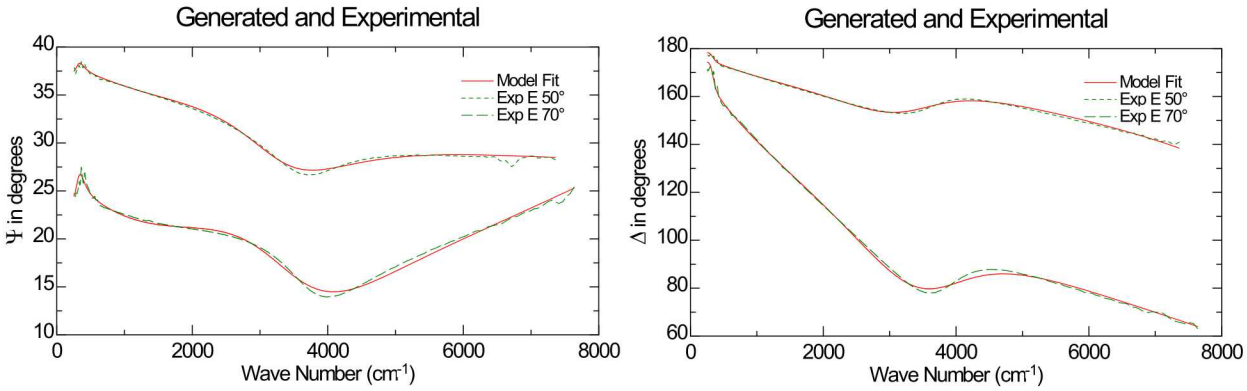

Figure 4-2. Raw and fitted ellipsometry data of sample PD170524-1c. This sample has ~87nm of In_2O_3 on a Si substrate. Red lines are the model, whereas dash lines are the raw data. The broad dip in ψ and Δ angles at around 4000 1/cm is from the Drude response of the carriers in the film.

Physical quantities such as carrier density and mobility were derived from the fit of the ellipsometry data based on the permittivity function model used. The confidence level of the quantities obtained depends on the quality of the fit and the accuracy of the model. The fit shown in Figure 4-2 has a mean square error (MSE) of 1.8. While this fit clearly captures all the main features of the data, there are still small discrepancies in the fit. This could be due to material quality or inadequacy of the model. In this fit, a Drude model is used to capture the properties of carriers in the sample, and an optical phonon model (TOLO) to capture the phonon features in the low frequency (< 1000 cm^{-1}) region. Since this is a rather thick film of 130 nm and high carrier density of $4x10^{20}$ cm^{-3}, the plasma feature is manifested in the strong variation in ψ and Δ angles around 4000 cm^{-1}. For this high carrier concentration and thick sample, the fitted concentration is not very sensitive to the quality of the phonon fit. A summary of some of the high-quality 2017 samples are shown in Table 4-1.

From the table, one can surmise that some samples (PD170601-2B and PD170524-2B) have complicated phonon spectrum and low carrier concentration. The confident level of the fitted concentrations of these samples are lower.

Table 4-1. Summary of some optical properties of In_2O_3 fabricated at Sandia. The numbers without error bar are the quantities not fitted. The dominant phonon mode of In_2O_3 is expected to be 300 1/cm, a more complete allowed modes can be found in [24].

	PD170601-1b_m2	PD170601-1c_m2	PD170601-2b_m3	PD170601-2c_m3	PD170524-2c_m1	PD170524-2b_m2
Ar/O2 flow (sccm)	40/0.5	40/0.5	400/1	40/1	40/2	40/2
Anneal condition	400 ℃ in air	400 ℃ in N_2	400 ℃ in air	400 ℃ in N_2	400 ℃ in N_2	400 ℃ in air
MSE	0.866	0.875	1.001	0.958	1.047	0.851
In_2O3 thickness (nm)	88.602 ±0.066	87.086 ±0.062	88.349 ±0.533	88.840 ±0.0689	92.09 ±0.08	91.953 ±0.725
In_2O_3 carrier density (1/cm^3)	4.3e19 ±4.2e18	4.9e19 ±2.3e18	4.9e19 ±5.5e18	5.5e19 ±4.2e18	3.7e19 ±2.5e18	1.9e19 ±1.2e19
In_2O_3 mobility (cm^2/Vs)	2.648 ±0.25	3.568 ±0.152	2.2716 ±0.25	2.441 ±0.18	4.303 ±0.256	2.997 ±1.99
TO 1 (1/cm)	363.19	364.9	361.83	365.03	362.07	330.95
TO 2 (1/cm)	409.27	411.08	414.18	409.56	409.3	451.24
TO 3 (1/cm)	600.49	603.45	592.94	605.53		605.05
LO 1 (1/cm)	387.66	383.62	411.87	381.5	403.69	
LO 2 (1/cm)			451.33			
LO 3 (1/cm)	533.55	517.25	592.94	531.49	564.11	519.34
LO 4 (1/cm)	603.16	603.8	623.4	606.47		662.82
LO 5 (1/cm)						750.94

To model the optical phonon properties, we use the TOLO model following the procedure given in Herzinger [25], where the permittivity function is written as

$$\epsilon(\omega) = \epsilon_\infty \prod_i \frac{\omega_{LO_i}^2 - \omega^2 - i\omega\gamma_{LO_i}}{\omega_{TO_i}^2 - \omega^2 - i\omega\gamma_{TO_i}},$$

where ω_{TO} and ω_{LO} are the transverse and longitudinal optical phonon frequencies respectively. Most phonon frequencies derived from the fit are consistent with published results such as Garcia-Domene et. al. [24].

4.3. Ellipsometric characterization of polycrystalline CdO

During this project, we also investigated the possibility of replacing In_2O_3 with CdO as the conductive oxide since it has much higher mobility which can translate to higher frequency operation and larger modulation depth with a shorter interaction length [9], [13]. For a similar carrier density, the mobility of CdO fabricated at Sandia was more than 10 times higher than In_2O_3.

As before, most of the films produced can be fitted with Drude and TOLO models with high fidelity. An example of a fit is shown in Figure 4-3.

We summarize the properties of other CdO film fabricated at Sandia in Table 4-2. Mobilities of ~100 cm^2/Vs and carrier densities of high 10^{19} to low 10^{20} cm^{-3} are commonly achieved without doping. Most samples also exhibit a high degree of uniformity along the growth direction. Among the films shown only one sample (mo49-co91) indicates nonuniformity behavior which requires an addition of a separate depletion layer to produce a good fit. These samples also have a MgO layer for protection. When the MgO layers are thick (mo43-co76, mo41-c075, mo41-co74), clear phonon features were observed, while for the thin ones (mo46-co86 and mo49-co91), these features are less certain. Discussion of these features is in the table caption.

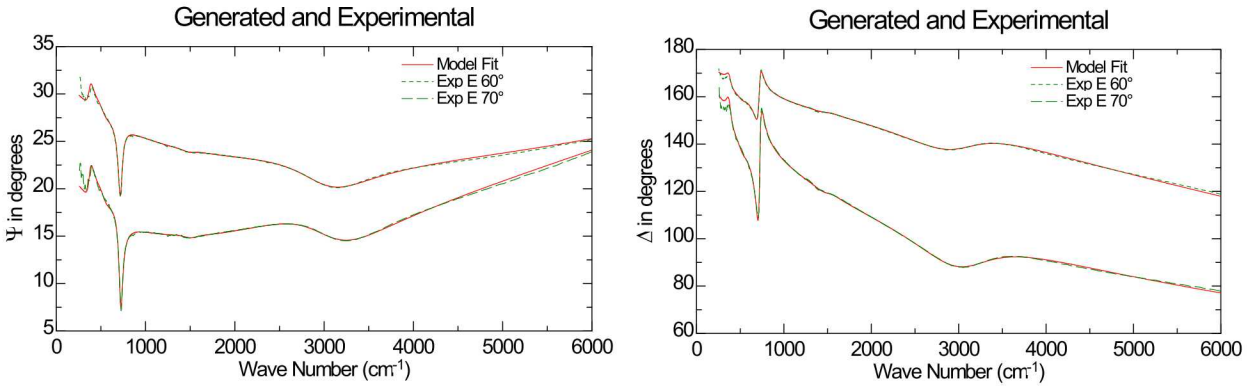

Figure 4-3. Raw and fitted ellipsometry data of sample mo41-co75. This sample has about 110nm of MgO on top of CdO deposited on a Si substrate. Red lines are the model, whereas dash lines are the raw data. The sharp feature at around 750 cm^{-1} in ψ and Δ angles is from the MgO phonon. The broad dip at around 3000 cm^{-1} in ψ and Δ angles is from the Drude response of the carriers in the CdO layer.

Table 4-2. Summary of some optical properties of CdO fabricated at Sandia. The numbers without error bar are the quantities not fitted. The strong transverse phonon of MgO is expected to be at 393 cm^{-1} and the longitudinal phonon is at 1070 cm^{-1} based on the fit of a bulk single crystal sample. The Wallis and two Fuchs-Kliewer modes [26] are expected to be at 520, 650, and 1354 cm^{-1}. Since the MgO film is not a single crystal, there is a certain amount of speculation in assigning these modes.

	M043-C076	M042-C075	M041-C074	M046-C086	M049-C091	M048-C090
MSE	1.814	1.372	1.48	1.479	3.061	3.45
CdO thickness (nm)	41.93 ±0.1	36.35 ±0.113	27.148 ±0.143	26.153 ±0.234	380.668 ±3.36	334.635 ±0.49
Log CdO carrier density ($1/cm^3$)	20.069 ±0.002	20.031 ±0.0027	20.048 ±0.004	19.843 ±0.005	19.479 ±0.002	19.475 ±0.001
CdO mobility (cm^2/Vs)	125.51 ±1.08	106.92 ±1.17	98.90 ±0.524	65.751 ±0.539	106.69 ±2.14	118.59 ±0.892
CdO TO (1/cm)	270.43	270.43	270.43		270	270
CdO LO (1/cm)	485	485	485		465	465
MgO thickness (nm)	107.67 ±0.173	110.19 ±0.163	94.46 ±0.198	8.969 ±0.521	2.92 ±2.9	52.315 ±0.773
MgO phonon 1 (1/cm)	389	379.29 ±1.02	389.5 ±0.459	284.9	393.1	491.77
MgO phonon 2 (1/cm)	570	584.91±2.1	570.51 ±3.54	608.38	644.74	657.52
MgO abs. feat. (1/cm)	1436.7	1479.7 ±4.89			1423.7	1209.4

This page left blank

5. PROGRAM IMPACT AND FUTURE WORK

The experimental and modeling work of this LDRD project have been well received by the integrated photonics community, generating more than 60 citations by the conclusion of the program and sparking a new wave of research and development on ENZ modulators. While earlier works developed the concept of ENZ modulation and provided critical early proof of the physics, the demonstration of gigahertz speed modulation in [5] acted to bring renewed interest into the promise of Si photonic modulations that break the bandwidth-size tradeoff without requiring exotic or unstable materials. We expect work in this area to continue to develop both inside and outside of Sandia.

The learnings of this program led to a new ENZ modulator design incorporated into silicon nitride waveguide platform for a more simplistic fabrication process and operation at shorter optical wavelengths. This new design was proposed as part of an ultra-low-power and dense photonic transceiver platform selected for funding under the DARPA PIPES program. This continuation funding will support fabrication of this updated modulator design and work to mature the technology by insertion into a full photonic system.

REFERENCES

[1] R. A. Soref and B. R. Bennett, "Electrooptical effects in silicon," IEEE J. Quant. Electron. **23**, 123 (1987).

[2] M. R. Watts, W. A. Zortman, D. C. Trotter, R. W. Young, and A. L. Lentine, "Low-voltage, compact, depletion-mode, silicon mach-zehnder modulator," IEEE J. Sel. Top. Quantum Electron. **16**, 159 (2010).

[3] Q. Xu, B. Schmidt, S. Pradhan, and M. Lipson, "Micrometre-scale silicon electro-optic modulator," Nature **435**, 325 (2005).

[4] M. G. Wood, J. R. Burr, and R. M. Reano, "7 nm/V DC tunability and millivolt scale switching in silicon carrier injection degenerate band edge resonators," Opt. Express **24**, 23481 (2016).

[5] M. G. Wood, S. Campione, S. Parameswaran, T. S. Luk, J. R. Wendt, D. K. Serkland, and G. A. Keeler, "Gigahertz speed operation of epsilon-near-zero silicon photonic modulators," Optica (2018).

[6] G. A. Keeler, K. M. Geib, D. K. Serkland, S. Parameswaran, T. S. Luk, J. R. Wendt, S. Campione, J. Ihlefled, and A. J. Grine, "High-speed operation of a compact ENZ electroabsorption modulator based on transparent conducting oxides," at Nanometa (2017).

[7] G. A. Keeler, K. M. Geib, D. K. Serkland, S. Parameswaran, T. S. Luk, A. J. Grine, J. Ihlefeld, S. Campione, and J. R. Wendt, "Multi-gigabit operation of a compact, broadband modulator based on ENZ confinement in indium oxide," at OFC (2017).

[8] G. A. Keeler, S. Campione, M. G. Wood, D. K. Serkland, S. Parameswaran, J. Ihlefeld, T. S. Luk, J. R. Wendt, and K. M. Geib, "Reducing optical confinement losses for fast, efficient, nanophotonic modulators," at IEEE Photonics Summer Topics (2017).

[9] S. Campione, M. G. Wood, D. K. Serkland, S. Parameswaran, J. Ihlefeld, T. S. Luk, J. R. Wendt, K. M. Geib, G. A. Keeler, "Sub-micrometer epsilon-near-zero electroabsorption modulators enabled by high-mobility cadmium oxide," IEEE Photon. J. (2017).

[10] M. G. Wood, S. Campione, D. K. Serkland, S. Parameswaran, J. Ihelfeld, T. S. Luk, J. R. Wendt, K. M. Geib, and G. A. Keeler, "High-mobility transparent conducting oxides for compact epsilon-near-zero silicon integrated optical modulators," at Frontiers in Optics (2017).

[11] S. Campione, M. G. Wood, S. Parameswaran, T. S. Luk, J. Wendt, D. Serkland, and G. A. Keeler, "Ultrafast epsilon-near-zero electroabsorption modulators," at APS/URSI (2018).

[12] T. S. Luk, M. G. Wood, and Y. Yang, "ENZ optical modulators," at IEEE RAPID (2018).

[13] I. C. Reines, M. G. Wood, T. S. Luk, D. K. Serkland, and S. Campione, "Compact epsilon-near-zero silicon photonic phase modulators," Opt. Express (2018).

[14] M. G. Wood, I. C. Reines, T. S. Luk, D. K. Serkland, S. Campione, "High-mobility transparent conducting oxides for compact epsilon-near-zero silicon photonic phase modulators," at CLEO (2019).

[15] S. Saha, S. Chowdhury, A. Dutta, N. Kinsey, A. Kildishev, V. M. Shalaev, A. Boltasseva, "Hybrid, long-range photonic-plasmonic interconnects with ultrathin TiN," at SPIE (2019).

[16]S. Saha, S. Chowdhury, A. Dutta, A. V. Kildishev, V. M. Shalaev, and A. Boltasseva, "Hybrid photonic-plasmonic waveguides with ultrathin TiN," at CLEO (2019).

[17]S. Saha, B. T. Diroll, J. Shank, Z. Kudyshev, A. Dutta, S. N. Chowdhury, T. S. Luk, S. Campione, R. D. Schaller, V. M. Shalaev, A. Boltasseva, M. G. Wood, "Broadband, high-speed, and large-amplitude dynamic optical switching with yttrium-doped cadmium oxide," Adv. Func. Mater., *accepted* (2019).

[18]X. Chen, C. Li, C. K. Y. Fung, S. M. G. Lo, and H.K. Tsang, "Apodized waveguide grating couplers for efficient coupling to optical fibers," IEEE Photon. Tech. Lett. **22**, 1156 (2010).

[19]M. G. Wood, L. Chen, J. R. Burr, and R. M. Reano, "Optimization of electron beam patterned hydrogen silsesquioxane mask edge roughness for low-loss silicon waveguides," J. Nanophoton. **8**, 083098 (2014).

[20]D. Ahn, C.-Y. Hong, J. Liu, W. Giziewicz, M. Baels, L. C. Kimerling, J. Michel, J. Chen, and F. X. Kärtner, "High performace, waveguide integrated Ge photodetectors," Opt. Express **15**, 3916 (2007).

[21]M. G. Wood, P. Sun, and R. M. Reano, "Compact cantilever couplers for low-loss fiber coupling to silicon photonic integrated circuits," Opt. Express **20**, 164 (2012).

[22]Y. Yang, K. Kelly, E. Sachet, S. Campione, T. S. Luk, J.-P. Maria, M. B. Sinclair, and I. Brener, "Femtosecond optical polarization switching using a cadmium oxide-based perfect absorber," Nat. Photonics **11**, 390 (2017).

[26]L. Savio, E. Celasco, L. Vattuone, M. Rocca, and P. Senet, "MgO/Ag(100): Confined vibrational modes in the limit of ultrathin films," Phys. Rev. B **67**, 075420 (2003).

[24]B. Garcia-Domene, H. M. Ortiz, O. Gomis, J. A. Sans, F. J. Manjón, A. Muñoz, P. Rodríguez-Hernández, S. N. Achary, D. Errandonea, D. Martínez-García, A. H. Romero, A. Singhal, and A. K. Tyagi, "High-pressure lattice dynamical study of bulk and nanocrystalline In_2O_3," J. Appl. Phys. **112**, p. 123511, 2012.

[23]B. Macco, Y. Wu, D. Vanhemel, and W. M. M. Kessels, "High mobility In2O3:H transparent conductive oxides prepared by atomic layer deposition and solid phase crystallization," Physica Status Solidi Rapid Res. Lett. **8**, 987 (2014).

[25]M. Schubert, T. E. Tiwald, and C. M. Herzinger, "Infrared dielectric anisotropy and phonon modes of sapphire," *Physical Review B,* vol. 61, pp. 8187-8201, 2000.

DISTRIBUTION

Email—Internal

Name	Org.	Sandia Email Address
Donna L. Chavez	01971	dchavez@sandia.gov
Technical Library	01177	libref@sandia.gov

This page left blank

Sandia National Laboratories

Sandia National Laboratories is a multimission laboratory managed and operated by National Technology & Engineering Solutions of Sandia LLC, a wholly owned subsidiary of Honeywell International Inc. for the U.S. Department of Energy's National Nuclear Security Administration under contract DE-NA0003525.